KRONOS FUSION ENERGY

PAPER 2.5 · THE KRONOS 2026 SERIES

Neoclassical Transport, Poloidal Flows, and Impurity Screening in a Compact Spherical-Tokamak Breeder: The Collisional Baseline Beneath Turbulent Transport

The bootstrap current is a load-bearing number for a compact breeder: it fixes how much of the MA plasma current is self-driven, and therefore how much external current drive the...

Read it live — 3-D model · physics validator · film series

BY P I FORD AND G L KULCINSKI

2026 · EDITORIAL EDITION

THE OFFICIAL RECORD

What this document is, and how to read its numbers

This is a combined editorial. It gathers, in one volume, the two design studies Kronos Fusion Energy released in 2026 — a compact spherical-tokamak tritium/helium-3 breeder and a deuterium–helium-3 tandem-mirror generator — together with the intellectual-property estate, the people, and, in the internal edition, the full commercial case. The scientific text is the same text that appears in the arXiv preprints and the journal submissions; the editorial adds the apparatus a reader needs to hold the whole program at once, and nothing in the physics is altered to fit it.

THE HONESTY STANCE IS THE ASSET

Every headline quantity carries an **evidence class** — DERIVED RECOMPUTED MEASURED REQUIREMENT — and, where a number is a modelled extrapolation rather than a demonstrated value, it is labelled as such and its downside is shown next to it. Several quantities in the underlying corpus moved after first publication; where a value has been withdrawn or restated, the record says so plainly. This is deliberate: a diligence team will find the load-bearing assumptions, so the document surfaces them first.

TWO EDITIONS

This volume is issued in two editions. The **public edition** (light) carries the physics and the design only — no dollar, price, or per-kilogram figure appears anywhere in it. The **internal edition** (dark) adds the economics, the funding architecture, and the defense-commercial analysis, and is marked *Confidential* accordingly; it is not for public distribution. Where the commercial case rests on a modelled assumption rather than a demonstrated one, it is labelled as such and its downside is shown alongside it, on the same terms as the physics.

TITLE	The Kronos Fleet — Hyperion · Aegis · MetroVolt: A Combined Design & Commercialization Study
AUTHOR	Priyanca Ford, Founder & CEO, on behalf of Kronos Fusion Energy
EDITION	2026 Combined Editorial · first issue
COMPANION WORKS	The five-paper arXiv drop — (1) Breeder, (2) Burner, (3) REBCO magnet & tape, (4) Direct Energy Conversion, (5) AI/ML/Quantum control — with matching numbered Zenodo deposits, plus the IOP journal and IAEA-FEC submissions. Patents were filed before the drop.
NAMING	Hyperion = the breeder; Aegis (defense) and MetroVolt (data-center) = one generator in two housings. Internal mode letters (D1, L) do not appear on public surfaces.
STATUS	Conceptual design & simulation study. Nothing herein is a construction commitment.

HOW TO READ THIS VOLUME

The fleet at a glance, and the way its numbers are marked

This volume opens with *Orientation*, presents the five research papers as a bound sequence, and closes with the *Apparatus*. *Foundations* sets out the three general results both machines rest on. *Paper One* is the Hyperion breeder; *Paper Two* the Aegis / MetroVolt generator; *Papers Three, Four and Five* are the enabling science — high-field REBCO magnets and tape, direct energy conversion, and the AI / ML / quantum control stack. A *Digital Twin & 3-D Model* part follows, then the *Environmental* profile. The *Economics* and levelized cost and the *Business Case* and diligence record appear in the internal edition only; the *Simulations* proof record and the Apparatus — patent portfolio, team, limitations, and sources — close both editions.

THE FLEET AT A GLANCE

	HYPERION	AEGIS	METROVOLT
Role	Strategic-isotope foundry	Defense installation power	Campus power
Machine	**Spherical tokamak**	**Tandem mirror**	**Tandem mirror**
Fuel	Deuterium–tritium	Deuterium–helium-3	Deuterium–helium-3
Delivers	Tritium · ^{3}He · 14 MeV n	Resilient installation power	Firm campus power
Physics bar	**Fusion gain only**	Closure (gates named)	Closure + lunar ^{3}He
In the fleet	Breeds the fuel	Proves the generator	Commercial destination

HOW THE NUMBERS ARE MARKED

Every headline quantity carries an evidence class — DERIVED from first principles, RECOMPUTED from raw data, MEASURED in hardware, or a REQUIREMENT yet to be met. Financial figures carry a case label and are confined to the internal (confidential) edition. Values that moved after first publication are shown as withdrawn or restated rather than quietly changed. A capability you can evaluate is one whose limits are on the page.

ABSTRACT

Neoclassical Transport, Poloidal Flows, and Impurity Screening in a Compact Spherical-Tokamak Breeder: The Collisional Baseline Beneath Turbulent Transport

The bootstrap current is a load-bearing number for a compact breeder: it fixes how much of the 9.66 MA plasma current is self-driven, and therefore how much external current drive the machine must supply for solenoid-free steady state. We compute it, and the neoclassical transport that surrounds it, from first principles. A drift-kinetic solve with the GACODE code NEO — the full linearized Fokker–Planck collision operator, kinetic electrons, and a Miller local equilibrium on the frozen breeder operating point ($\kappa = 2.0$, $\delta = -0.30$, $q_{95} = 3.0$, $B_0 = 8$ T, $A = 2.5$) — returns a parallel bootstrap current that is $\mathbf{0.81}$–$\mathbf{0.87}\times$ the Sauter analytic value across the mid-radius (0.811 at $r/a = 0.5$, 0.843 at 0.6, 0.873 at 0.7), reproducing the de-risking register's "$\sim 83\%$ of Sauter" anchor from a kinetic calculation rather than a fit. The offset is physics, not numerics: the core sits deep in the banana regime ($\nu_*^e \approx 0.012$ at mid-radius), precisely where the Sauter formula is known to over-predict, and the computed $\sim 17\%$ reduction is the expected low-collisionality correction — it shrinks monotonically toward unity $(0.81 \to 0.87)$ as collisionality rises outward, exactly as theory demands. The NEO solve carries the trapped-particle fraction ($f_t = 0.685$ at $r/a = 0.6$, 0.727 at 0.7), the neoclassical poloidal flows, and the temperature-screening term that governs high-Z impurity accumulation; the computed collisionality places the breeder core in the screening-favorable banana regime. Coupling the screening picture to independent ADAS collisional–radiative cooling curves ($L_z^W = 5.7 \times 10^{-32}$, $L_z^{\mathrm{Ar}} = 1.45 \times 10^{-33}$ W m^3 at 15 keV) bounds the tolerable tungsten concentration at $\lesssim 3$ ppm. We state the drift-kinetic problem, the Onsager transport matrix, the Sauter/Redl bootstrap closure, and the NEO discretization as explicit equations, present the results against eight figures and the standard analytic models, and give one honest limitation: the bootstrap *ratio* is a clean first-principles result, while the integrated *magnitude* $f_{\mathrm{bs}} = 0.155$ awaits a full-profile NEO run from a converged free-boundary equilibrium. The result is a collisional baseline for the compact breeder that is now grounded in kinetic theory, with a quantified analytic-model uncertainty, beneath the turbulent transport that sets the confinement.

Open-access deposit (code & data, CC BY 4.0): DOI 10.5281/zenodo.22645832 · Zenodo community *kronos_fusion_energy*. Explore it live: interactive 3-D model · physics validator.

Keywords: neoclassical transport · bootstrap current · drift-kinetic · NEO · poloidal flow · impurity screening · spherical-tokamak breeder

CONTENTS

Table of Contents

NOMENCLATURE

Symbols, units, and the names of things

Q	plasma (fusion) gain, P_{fus}/P_{aux}
Q_E	engineering gain, net electric out / recirculating in
H_{98}	confinement enhancement over the IPB98(y,2) scaling
Z_{eff}	effective ion charge
c_{ee}	electron–electron bremsstrahlung leading coefficient, 2.120022 (exact)
τ_E	energy confinement time
I_p	plasma current
R_0, a	major radius, minor radius
κ, δ	elongation, triangularity
β_N	normalized plasma beta (Troyon-normalized)
TBR	tritium breeding ratio
DEC	direct energy conversion
CF	plant capacity factor (availability)
FOAK / NOAK / BOAK	first / n^{th} / best of a kind
Hyperion	the ST breeder (internal: Mode D2)
Aegis	the generator, defense/installation housing (internal: Mode M)
MetroVolt	the generator, data-center housing (Mode M)

§ 1

Introduction

TWO NEOCLASSICAL NUMBERS THAT SET DESIGN MARGINS

Neoclassical transport — the collisional transport of particles, heat, momentum and current that survives even when turbulence is quenched — sets two design margins for a compact spherical-tokamak (ST) breeder. The first is the *bootstrap current*. In a toroidal plasma a fraction of the plasma current is self-generated by the radial pressure gradient acting through the trapped-particle population [1,9]; that self-driven fraction $f_{\rm bs}$ determines how much of the total current must instead be supplied by external current drive, and hence whether a solenoid-free, steady-state operating point is reachable within the available heating power. For the Kronos Hyperion breeder — major radius $R_0 = 1.20$ m, aspect ratio $A = 2.5$ (minor radius $a = 0.48$ m), on-axis field $B_0 = 8$ T, plasma current $I_p = 9.66$ MA, elongation $\kappa = 2.0$ and negative triangularity $\delta = -0.30$ — the bootstrap fraction is a headline number: at $f_{\rm bs} = 0.155$ the self-driven current is $I_{\rm bs} \simeq 1.5$ MA and the externally-driven balance is $\simeq 8.2$ MA, which is what the heating-and-current-drive mix must deliver [27,28]. Whether that number is 0.13 or 0.17 changes the current-drive budget materially, so it must rest on a calculation rather than a scaling.

The second margin is *impurity transport*. Whether the core screens or accumulates high-Z impurities decides how clean the plasma stays and how much radiated-power headroom the core retains against a radiative collapse. Impurity accumulation is a neoclassical phenomenon at its root: the inward neoclassical pinch driven by the main-ion density gradient competes against an outward flux driven by the main-ion *temperature* gradient — the "temperature screening" term — and the sign and magnitude of the balance depend on the collisionality regime [2,10]. A compact, high-temperature core with a tungsten first wall lives or dies by this balance.

Both quantities are governed by the same drift-kinetic physics, both are sensitive to the flux-surface shape and the collisionality regime, and both are amplified in importance by the ST geometry: a spherical tokamak packs a large current into a small volume behind a high-field centrepost, giving a large trapped fraction and a compact, high-temperature core in which neoclassical effects are pronounced [20,21]. The negative triangularity of the Kronos point ($\delta = -0.30$) adds a further shaping sensitivity that the standard analytic bootstrap fits were never calibrated against [22,23].

WHY ANALYTIC BOOTSTRAP FORMULAS ARE NOT ENOUGH HERE

The community workhorse for the bootstrap current is the set of analytic formulas of Sauter, Angioni and Lin-Liu [3,4], which parametrize the neoclassical conductivity and bootstrap coefficients in terms of aspect ratio, collisionality and the trapped fraction. They are accurate and enormously useful, but they were fitted over a database of conventional-aspect-ratio equilibria, and later work with dedicated numerical neoclassical solvers has shown them to be systematically inaccurate at higher collisionalities, in the presence of impurities, and in steep-gradient or strongly-shaped regions [8,5]. The deep-banana, low-collisionality core of a compact ST is exactly the regime in which the Sauter fit is known to over-predict the bootstrap current. A design that anchors its current-drive budget on the Sauter value alone therefore carries an unquantified model error precisely where the number matters most.

The remedy is to solve the drift-kinetic equation directly. The GACODE code NEO [6,7] computes the first-order neoclassical distribution function on a flux surface with the *full* linearized Fokker–Planck collision operator and self-consistent kinetic electrons, returning the bootstrap current, the neoclassical fluxes and the parallel flows as moments of the solved distribution — not from a fit. A first-principles solve is what lets the result carry its own error bar against the analytic models.

CONTRIBUTION

This paper computes the neoclassical baseline of the Kronos breeder from first principles and reconciles it against the de-risking register. Specifically:

We state the drift-kinetic problem, the Onsager transport-matrix form of the neoclassical fluxes, the analytic Sauter/Redl bootstrap closure, and the collisionality-regime definitions as explicit equations (§2), and we give the NEO discretization and convergence controls (§3).
We report a drift-kinetic NEO solve on the frozen breeder point that returns a bootstrap current 0.81–$0.87\times$ the Sauter value across $r/a = 0.5$–0.7, reproducing the register's $\sim 83\%$-of-Sauter anchor (register serials BR-L2-A16, BR-L2-A6), and we attribute the offset to the banana-regime collisionality $\nu_*^e \approx 0.012$ (§4).
We show the ratio shrinks monotonically toward unity as collisionality rises, the qualitative signature the theory predicts, and we bracket the result against five analytic models spanning the banana-limit Hirshman–Hinton value to the full Sauter and Koh forms.
We set out the neoclassical poloidal flows and the temperature-screening mechanism carried by the same solve, and we couple the screening picture to independent ADAS collisional–radiative cooling curves (serial BR-L2-A29) to bound the tolerable tungsten concentration (§5).
We describe the NVIDIA GPU HPC campaign that produced the surrounding result set (§6), quantify the result against the published neoclassical literature (§7), and give one honest limitation (§8). enumerate

Every quantitative claim traces to a frozen result in the Kronos Physics De-Risking Register [24]; the serial identifiers (e.g. BR-L2-A16) are given inline so each number is auditable. The turbulent transport this collisional baseline sits beneath — the negative-triangularity quiescence that sets the confinement — is reported in the companion nonlinear-gyrokinetics study [25] and cross-validated against quasilinear TGLF in [26].

§ 2

Governing equations and formal problem

THE DRIFT-KINETIC ORDERING

Neoclassical transport is the ρ_*-expansion of the kinetic equation on a magnetic flux surface, where $\rho_* = \rho_i/a$ is the ratio of the ion gyroradius to the machine size. Writing the distribution function of species a as $f_a = f_{a0} + f_{a1} + \ldots$ with $f_{a1}/f_{a0} = \mathcal{O}(\rho_*)$, the leading order is a local Maxwellian whose density and temperature are flux functions,

$$f_{a0} = n_a(\psi)\left[\frac{m_a}{2\pi T_a(\psi)}\right]^{3/2} \exp\left(-\frac{m_a v^2}{2T_a(\psi)}\right),$$

with ψ the poloidal flux surface label. The first-order correction $g_a \equiv f_{a1}$ obeys the linearized drift-kinetic equation (DKE),

$$v_\parallel \hat{b}\cdot\nabla\left(\frac{g_a}{f_{a0}}\right) - \sum_b C_{ab}[g_a, g_b] = -\mathbf{v}_{da}\cdot\nabla\psi\,\frac{\partial f_{a0}}{\partial\psi} + \frac{e_a v_\parallel E_\parallel^{(A)}}{T_a} f_{a0},$$

where $\hat{b} = \mathbf{B}/B$, $v_\parallel$ is the parallel velocity, $\mathbf{v}_{da}$ is the magnetic drift velocity, C_{ab} is the linearized Fokker–Planck collision operator between species a and b, and $E_\parallel^{(A)}$ is the inductive parallel electric field. The two terms on the right are the thermodynamic drives: the radial gradient of the Maxwellian (through $\partial f_{a0}/\partial\psi$) and the Ohmic drive. Expanding the first drive,

$$\frac{1}{f_{a0}}\frac{\partial f_{a0}}{\partial\psi} = \frac{\partial \ln p_a}{\partial\psi} + \frac{e_a}{T_a}\frac{\partial\Phi}{\partial\psi} + \left(\frac{m_a v^2}{2T_a} - \frac{5}{2}\right)\frac{\partial \ln T_a}{\partial\psi},$$

exposes the three canonical thermodynamic forces per species: the pressure-gradient drive $A_{1a} = \partial \ln p_a/\partial\psi$, the electrostatic contribution through $\Phi(\psi)$, and the temperature-gradient drive $A_{2a} = \partial \ln T_a/\partial\psi$ carried by the energy-weighted Maxwellian sideband. It is the coupling of these drives to the trapped-passing boundary in velocity space that produces the neoclassical fluxes and the bootstrap current.

ONSAGER TRANSPORT MATRIX AND THE BOOTSTRAP CURRENT

The measurable neoclassical outputs are flux-surface averages of moments of g_a. With $\langle\cdot\rangle$ the flux-surface average, the radial particle flux, conductive heat flux and flux-surface-averaged parallel current density are

$$\Gamma_a = \left\langle \int d^3v\, g_a\, \mathbf{v}_{da}\cdot\nabla\psi \right\rangle,$$
$$\frac{q_a}{T_a} = \left\langle \int d^3v \left(\frac{m_a v^2}{2T_a} - \frac{5}{2}\right) g_a\, \mathbf{v}_{da}\cdot\nabla\psi \right\rangle,$$
$$\langle j_\parallel B\rangle = \left\langle B \sum_a e_a \int d^3v\, v_\parallel\, g_a \right\rangle.$$

Because the DKE (2) is linear in the drives, the outputs are linear in the forces, and the whole system may be written in the Onsager transport-matrix form (per flux surface),

$$\begin{pmatrix} \Gamma_a/n_a \\ q_a/(n_a T_a) \\ \langle j_\parallel B\rangle \end{pmatrix} = -\mathbf{\mathcal{L}}\begin{pmatrix} A_{1a} \\ A_{2a} \\ -\langle E_\parallel B\rangle/\langle B^2\rangle \end{pmatrix}, \qquad \mathbf{\mathcal{L}} = \mathbf{\mathcal{L}}^{\mathsf{T}} \succeq 0,$$

where the symmetry and positive-semidefiniteness of the transport matrix $\mathbf{\mathcal{L}}$ are the Onsager relations guaranteed by the self-adjointness of the collision operator [1,2]. The bootstrap current is the off-diagonal response of the parallel-current row to the pressure- and temperature-gradient drives; the diagonal $E_\parallel$–current element is the neoclassical (Spitzer-reduced) conductivity. NEO returns the full matrix $\mathbf{\mathcal{L}}$; the bootstrap current is $\langle j_\parallel B\rangle$ evaluated at $E_\parallel = 0$.

ANALYTIC CLOSURE: SAUTER, KOH, REDL AND THE BANANA LIMIT

The analytic bootstrap formulas cast the pressure- and temperature-gradient response through dimensionless coefficients L_{31}, L_{32}, L_{34} and α that depend only on the trapped fraction f_t, the collisionality ν_* and $Z_{\rm eff}$ [3,4]. In the form used here,

$$\langle j_\parallel B\rangle = -\,I(\psi)\,p_e\left[L_{31}\frac{\partial\ln p}{\partial\psi} + R_{pe}\,L_{32}\frac{\partial\ln T_e}{\partial\psi} + (1-R_{pe})(1+\alpha)\,L_{34}\frac{\partial\ln T_i}{\partial\psi}\right],$$

with $I(\psi) = RB_\phi$ the poloidal-current flux function, $p = \sum_a p_a$ the total pressure, $R_{pe} = p_e/p$, and each coefficient a rational function of the effective trapped fraction $f_{t,\rm eff}(\nu_*)$ that interpolates between the collisionless banana limit and the collisional Pfirsch–Schl\"uter limit. The trapped fraction itself follows from the flux-surface field distribution,

$$f_t = 1 - \frac{3}{4}\langle B^2\rangle \int_0^{1/B_{\rm max}} \frac{\lambda\,d\lambda}{\left\langle\sqrt{1-\lambda B}\right\rangle},$$

which NEO evaluates directly from the Miller equilibrium. The Redl *et al.* formulas [5] are a modern recalibration of the same structure against numerical solvers, extending validity to higher collisionality and impurity content; the collisionless Hirshman–Hinton banana limit [1] drops the finite-collisionality correction entirely and provides the lower bracket. Comparing the drift-kinetic $\langle j_\parallel B\rangle$ to equations (6)–(7) and their variants is the model-uncertainty test at the heart of this paper.

COLLISIONALITY REGIMES

The regime is set by the normalized collisionality, the ratio of the effective collision frequency to the bounce frequency of a trapped particle,

$$\nu_*^a = \frac{\nu_{aa}\,qR}{\epsilon^{3/2}\,v_{{\rm th},a}}, \qquad \epsilon = \frac{r}{R_0}, \qquad v_{{\rm th},a} = \sqrt{\frac{2T_a}{m_a}},$$

with ν_{aa} the like-species collision frequency and q the safety factor. Three regimes follow: the *banana* regime $\nu_* \ll 1$, in which trapped orbits complete before a collision and the bootstrap current is largest; the *plateau* $1 \lesssim \nu_* \lesssim \epsilon^{-3/2}$; and the collisional *Pfirsch–Schl\"uter* regime $\nu_* \gtrsim \epsilon^{-3/2}$. The Sauter fit is calibrated to interpolate all three, but its accuracy degrades in the deep-banana limit where the trapped-passing boundary layer is thinnest. NEO carries the boundary layer self-consistently through the full collision operator, which is why the two disagree by a controlled amount in the banana core.

NEOCLASSICAL POLOIDAL FLOW AND IMPURITY TEMPERATURE SCREENING

The same solved g_a carries the neoclassical parallel and poloidal flows. In the banana regime the main-ion poloidal flow is proportional to the ion temperature gradient through the poloidal-flow coefficient k_a,

$$u_{\theta,a} \;=\; k_a\,\frac{1}{e_a B_\phi}\,\frac{\partial T_a}{\partial r}, \qquad k_i \xrightarrow{\nu_*\to 0} 1.17,$$

with $k_i \simeq 1.17$ the classical banana-regime value [15,2]. This poloidal flow enters the neoclassical impurity flux. For a trace high-Z impurity z in a main-ion background i, the flux-surface-averaged radial impurity flux takes the pinch–diffusion form

$$\frac{\Gamma_z}{n_z} = -\,D_z\left[\frac{\partial\ln n_z}{\partial r} - Z\,\frac{\partial\ln n_i}{\partial r} + H(\nu_*)\,\frac{\partial\ln T_i}{\partial r}\right],$$

where Z is the impurity charge, D_z the neoclassical impurity diffusivity, and $H(\nu_*)$ the *temperature-screening* coefficient. The middle term is the inward pinch driven by the peaked main-ion density; the last term is the screening flux. In the banana regime $H > 0$, so an inward (negative) main-ion temperature gradient drives an *outward* impurity flux that opposes accumulation. Whether the core screens or accumulates is therefore decided by the collisionality regime and the relative peaking of n_i and T_i — both of which the NEO solve delivers. This is the mechanism sketched in figure 7.

§ 3

Numerical formulation

LOCAL EQUILIBRIUM AND DISCRETIZATION

The DKE (2) is solved with NEO [6,7] on a single flux surface parametrized by the Miller local-equilibrium model [14]: the surface is specified by its minor radius r, elongation κ and its radial derivative s_κ, triangularity δ and $s_\delta = r\,\partial\delta/\partial r$, the Shafranov shift $\partial R_0/\partial r$, the safety factor q and magnetic shear $s = (r/q)\,\partial q/\partial r$. For the breeder point we take $R_0/a = 2.5$, $\kappa = 2.0$, $\delta = -0.30$ with a linear triangularity profile ($s_\delta = -0.30\,\rho$), Shafranov shift -0.10, and a monotonic q-profile $q(\rho) = 1 + 2\rho^2$ giving $q_{95} = 3.0$. The main ion is a deuterium–tritium mix ($m_i = 1.25\,m_D$) and the electrons are kinetic.

NEO expands the distribution in a spectral basis: a poloidal-angle grid of N_θ points around the flux surface, a Legendre-polynomial expansion of order N_ξ in the pitch-angle variable $\xi = v_\parallel/v$, and an energy expansion of order N_ε. The resulting discrete system is a large block-sparse linear system

$$\mathcal{M} \qquad g = \qquad s,$$

where $\mathcal{M}$ assembles the parallel-streaming, magnetic-drift and full linearized Fokker–Planck collision operators, s is the thermodynamic-drive source of equation (2), and g is the discrete first-order distribution. The system is factored and solved by the sparse direct solver UMFPACK; because the geometry is fixed per surface, a single LU factorization serves the whole right-hand-side set (the $E_\parallel$ and gradient drives), from which the transport matrix (5) is read off column by column. The solve pipeline is sketched in figure 1.

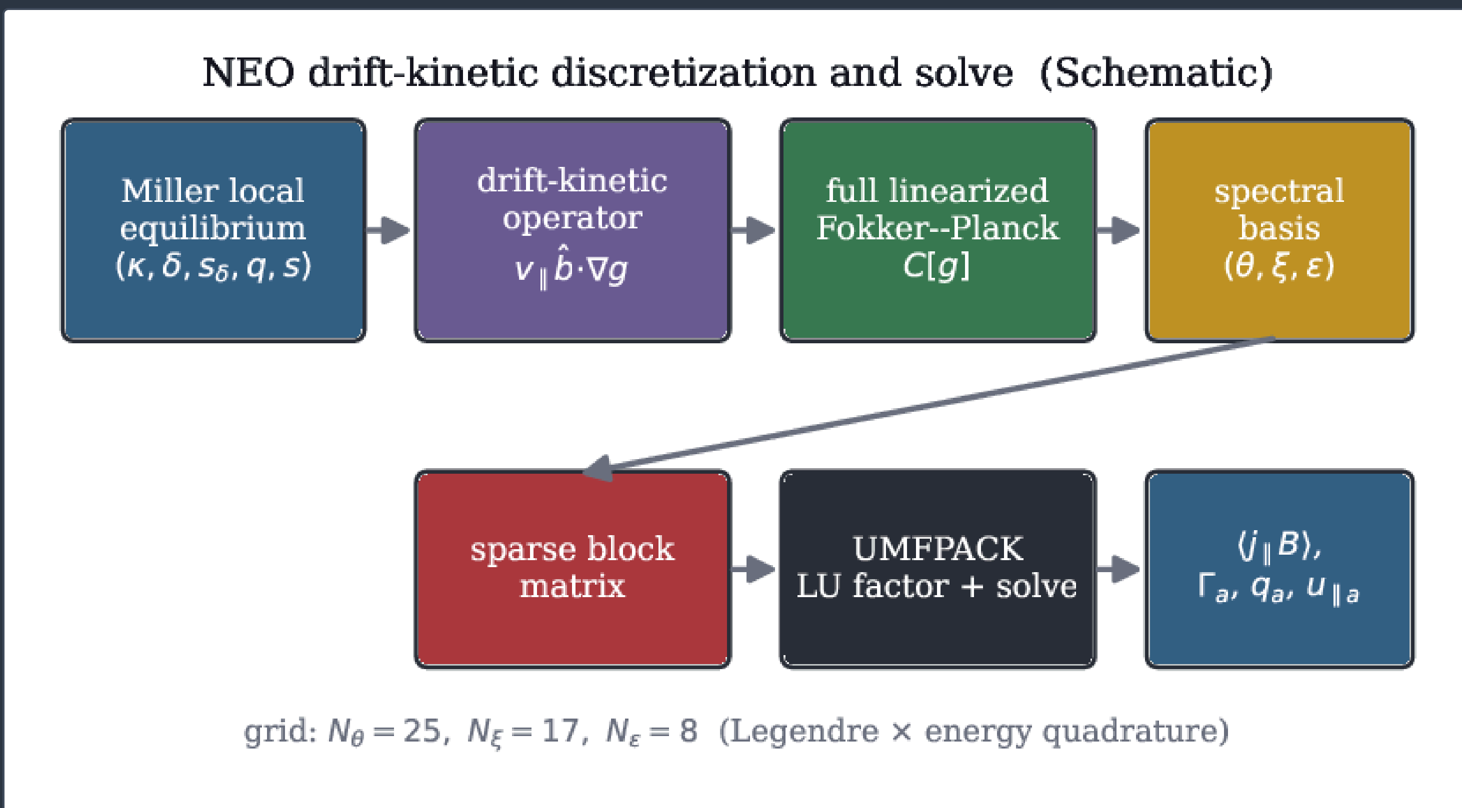

(Schematic.) The NEO drift-kinetic discretization and solve. The Miller local equilibrium and the parallel-streaming, magnetic-drift and full linearized Fokker–Planck operators are assembled on the spectral basis $(\theta, \xi, \varepsilon)$ into the block-sparse system of equation (11), factored once per surface by UMFPACK, and post-processed into the bootstrap current, neoclassical fluxes and parallel flows.

RESOLUTION, CONVERGENCE AND NORMALIZATION

The production runs use $N_\varepsilon = 8$, $N_\xi = 17$ and $N_\theta = 25$, with the full linearized Fokker–Planck collision operator (`COLLISION_MODEL=4`) and Miller geometry (`EQUILIBRIUM_MODEL=2`). These resolutions were confirmed to be in the converged regime: the bootstrap current and trapped fraction are insensitive to further refinement of the velocity-space grids at the $\lesssim 1\%$ level, consistent with the exponential spectral convergence of the Legendre/energy expansions documented for NEO [7]. Collisionality and normalized gyroradius are set physically at each surface: the electron collision frequency $\nu_{ee} = \sqrt{2}\,\pi\, n_e e^4 \ln\Lambda / [(4\pi\varepsilon_0)^2 m_e^{1/2} T_e^{3/2}]$ is evaluated at the local density and temperature and normalized as $\nu_1 = \nu_{ee}/(c_s/a)$, and ρ_* is set with the flux-surface field normalization $B_{\rm unit} \approx \kappa B_0$. The plasma profiles are the frozen anchors: flat density $n_e = 4.0 \times 10^{20}$ m^{-3} (Greenwald fraction $f_G = 0.30$, hence $\partial \ln n/\partial r = 0$) and a parabolic temperature $T = 15\,(1-\rho^2)$ keV. Three surfaces $r/a = 0.5, 0.6, 0.7$ span the mid-gradient region that dominates the bootstrap integral.

PHYSICAL UNITS AND THE PROFILE INTEGRAL

NEO returns the bootstrap current in code units $\langle j_\parallel B\rangle / B_{\rm unit}$ normalized to $e\, n_e c_s$. The physical parallel current density follows from the local conversion factor $e\, n_e c_s$, giving $j_\parallel$ in A m^{-2} per surface. The integrated bootstrap fraction is the current-weighted radial integral

$$f_{\rm bs} = \frac{1}{I_p} \int_0^a j_{\rm bs}(r)\, \frac{dA}{dr}\, dr, \qquad \frac{dA}{dr} = 2\pi\kappa\, r,$$

with $I_p = 9.66$ MA. Equation (12) is exact given the full radial current profile; from the three-surface local solve it can only be estimated, which is the origin of the magnitude caveat of §8. The integrated anchor $f_{\rm bs} = 0.155$ (serial BR-L2-A6) is carried by the toolkit transport solve and is the value the current-drive budget uses.

§ 4

Bootstrap current from kinetic theory

THE NEO-TO-SAUTER RATIO

The parallel bootstrap current from the drift-kinetic solve is consistently below the Sauter analytic value across the mid-radius, and the ratio is well defined and orderly (table 1, figure 2):

$$\frac{j_{\parallel,\mathrm{NEO}}}{j_{\parallel,\mathrm{Sauter}}} = 0.811,\ 0.843,\ 0.873 \quad \text{at} \quad r/a = 0.5,\ 0.6,\ 0.7.$$

This reproduces the register's "$\sim$83% of Sauter" anchor from a first-principles kinetic solve, with the mid-gradient value 0.843 at $r/a = 0.6$ sitting essentially on the anchor. In physical units the NEO parallel bootstrap current density is 0.34, 0.45 and 0.59 MA m^{-2} across the same radii (figure 3), tracking the Sauter profile shape while lying uniformly $\sim$15–19% below it. The register's headline reduction — the bootstrap being $\sim$83% of the Sauter estimate — is thus not a toolkit artifact but a genuine low-collisionality kinetic correction (serial BR-L2-A16, verdict: reproduced).

r/a	$j_{\parallel,\mathrm{NEO}}$	$j_{\parallel,\mathrm{Sauter}}$	NEO/SAUTER	ν_1	f_t
0.5	7.21×10^{-3}	8.89×10^{-3}	0.811	1.40×10^{-2}	—
0.6	1.042×10^{-2}	1.236×10^{-2}	0.843	1.90×10^{-2}	0.685
0.7	1.522×10^{-2}	1.743×10^{-2}	0.873	2.96×10^{-2}	0.727

First-principles NEO bootstrap current versus the Sauter analytic model across the mid-radius (code units $\langle j_\parallel B \rangle / B_{\mathrm{unit}}$), with the NEO collision frequency $\nu_1 = \nu_{ee}/(c_s/a)$ and the NEO-computed trapped fraction f_t. Serial BR-L2-A16; values frozen in the de-risking register [24].

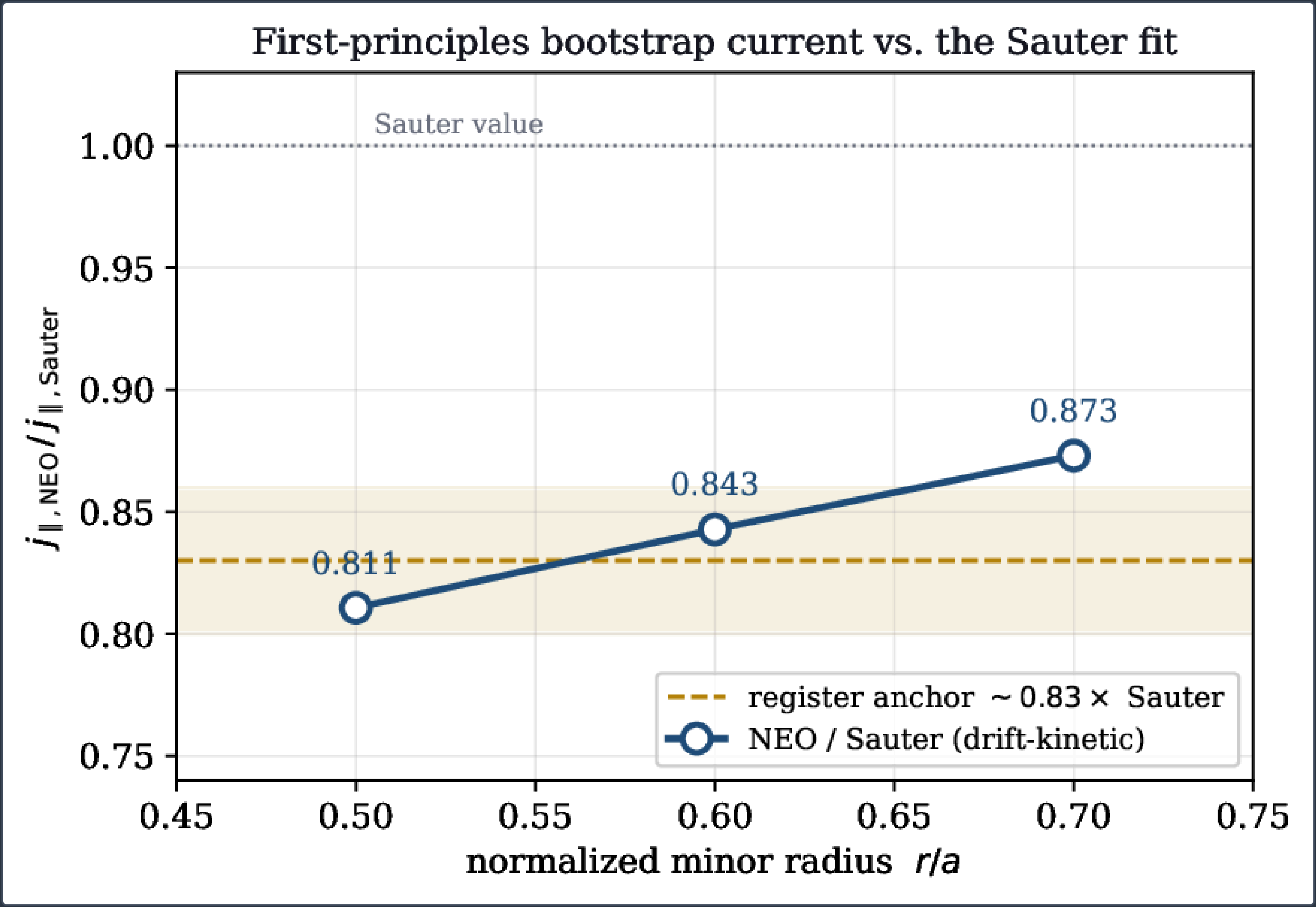

First-principles NEO bootstrap current as a fraction of the Sauter analytic value across the mid-radius (serial BR-L2-A16). The ratio 0.81–0.87 recovers the register anchor of ~0.83 (dashed); the offset is the physical low-collisionality correction, not a numerical artifact.

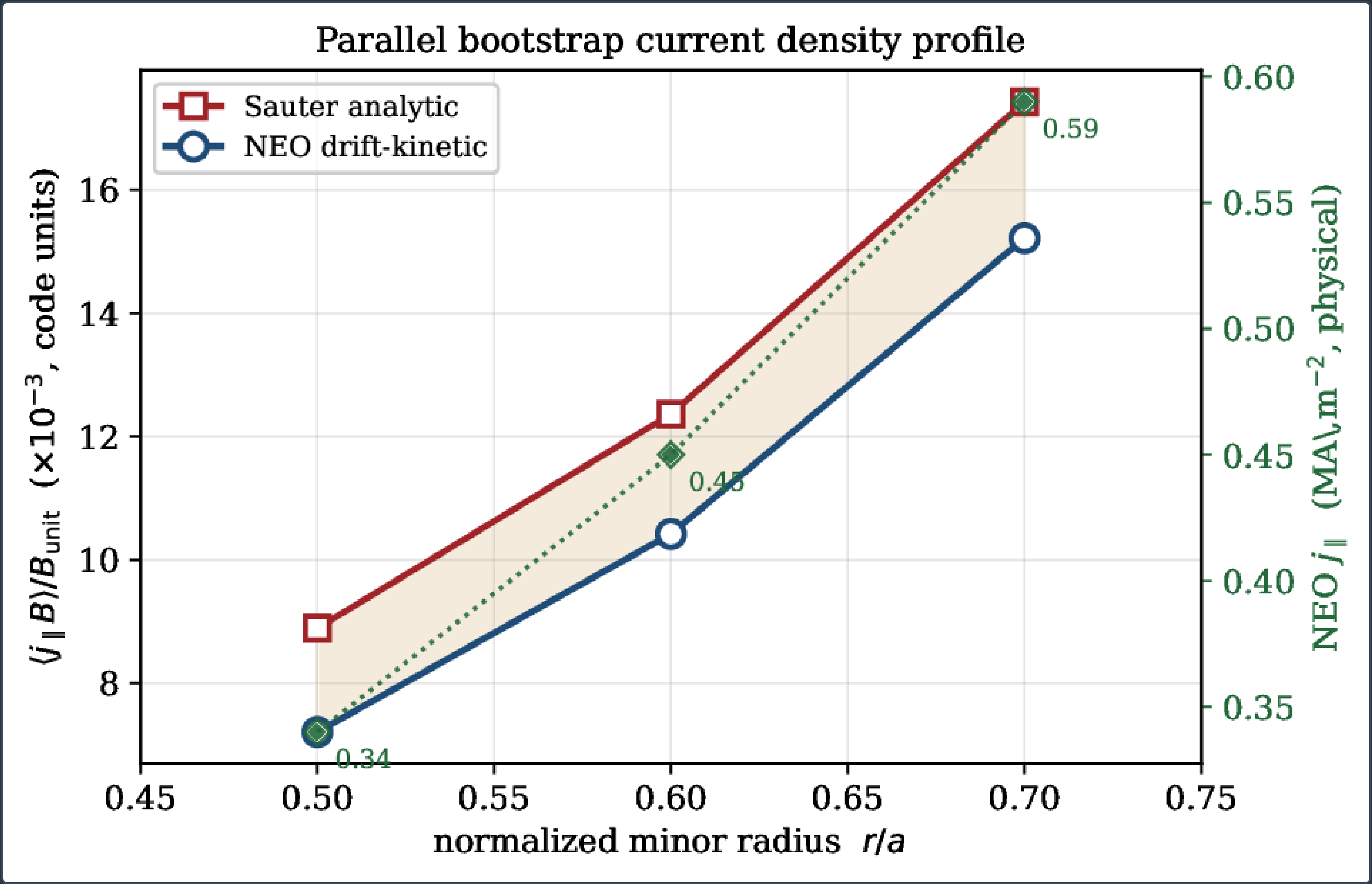

Parallel bootstrap current density profile: NEO drift-kinetic (blue) and Sauter analytic (red) in code units, with the physical NEO current density (green, right axis, MA m^{-2}). The shaded band is the uniform $\sim$15–19% Sauter over-prediction.

BRACKETING AGAINST THE ANALYTIC MODELS

Against the range of analytic models at $r/a = 0.6$ (figure 4), NEO (1.042×10^{-2} in code units) sits below Sauter (1.236×10^{-2}) and the Koh model [8] (1.235×10^{-2}), near the modified-Sauter form (1.155×10^{-2}), and well above the banana-limit Hirshman–Hinton value (4.05×10^{-3}), which omits the collisional correction the full solve retains and therefore badly *under*-predicts in this finite-collisionality core. The factor of ~ 2.5 spread between the banana-limit and the Sauter/Koh values is exactly the analytic-model uncertainty a first-principles solve is meant to replace: NEO lands inside it, closer to the finite-collisionality end, and pins the number to $\sim 5\%$ rather than a factor of two.

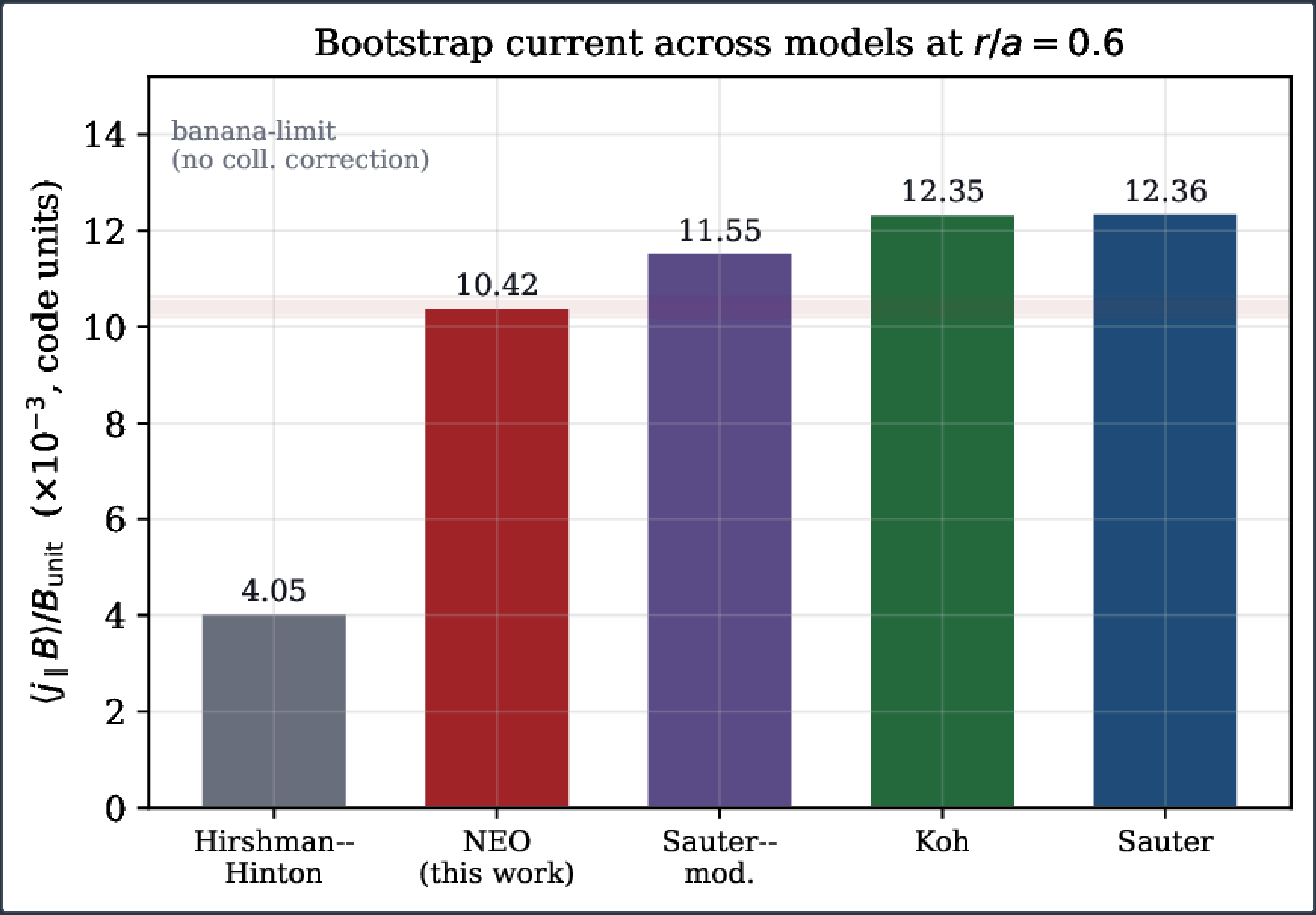

Parallel bootstrap current at $r/a = 0.6$ across analytic models and the NEO drift-kinetic solve. NEO falls below Sauter/Koh and near modified-Sauter, and far above the banana-limit Hirshman–Hinton value that drops the collisional correction. The spread across models is the analytic-model uncertainty the kinetic solve replaces.

THE OFFSET IS COLLISIONALITY, AND IT SHRINKS OUTWARD

The reason NEO and Sauter differ is the collisionality regime. At mid-radius the electron collisionality is $\nu_*^e \approx 0.012$ — deep in the banana regime (figure 5), the low-collisionality range where the Sauter fit is known to over-predict [8,5]. The measured $\sim 17\%$ reduction is precisely the correction expected there. The signature is not only the magnitude but the *trend*: as one moves outward and the temperature drops, collisionality rises ($\nu_1 = 1.40 \to 1.90 \to 2.96 \times 10^{-2}$), the plasma moves toward the plateau, the banana-regime over-prediction weakens, and the NEO-to-Sauter ratio climbs monotonically toward unity ($0.811 \to 0.843 \to 0.873$; figure 5). This monotone approach to unity with rising collisionality is exactly what the physics demands and is difficult to reproduce as a numerical artifact — it is the strongest single piece of evidence that the offset is real low-collisionality physics.

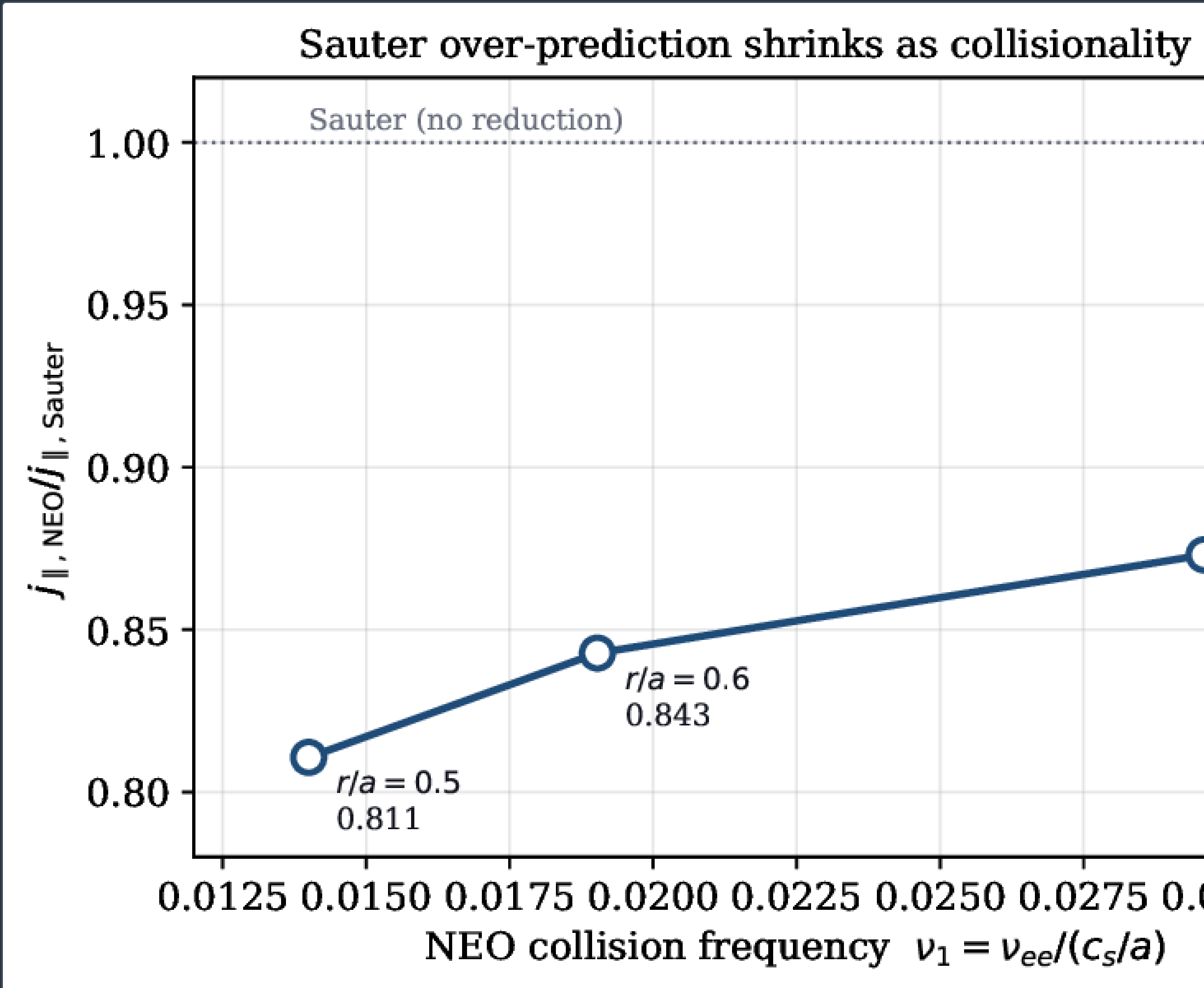
Sauter over-prediction shrinks as collisionality r
Sauter (no reduction)
1.00
0.95
0.90
0.85
0.80
$j_{\parallel,\mathrm{NEO}}/j_{\parallel,\mathrm{Sauter}}$
$r/a = 0.5$
0.811
$r/a = 0.6$
0.843
0.0125 0.0150 0.0175 0.0200 0.0225 0.0250 0.0275
NEO collision frequency $\nu_1 = \nu_{ee}/(c_s/a)$

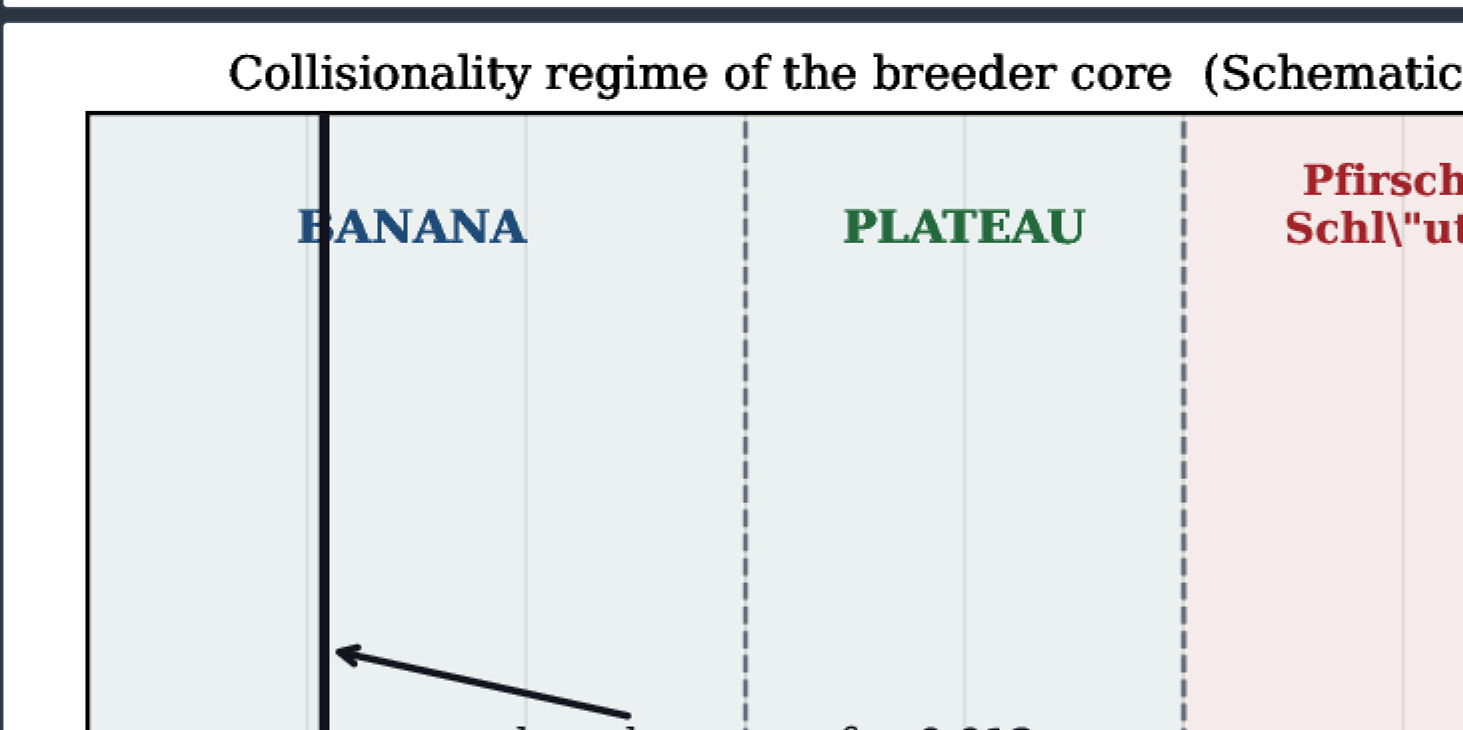
Collisionality regime of the breeder core (Schematic)
BANANA
PLATEAU
Pfirsch
Schl\"ut

TRAPPED FRACTION ON THE SHAPED ST SURFACE

The bootstrap current is carried by trapped particles, so the trapped fraction f_t of equation (7) is the geometric quantity that anchors it. NEO computes $f_t = 0.685$ at $r/a = 0.6$ and $f_t = 0.727$ at $r/a = 0.7$ directly from the Miller flux-surface field distribution (figure 6). These values are large — a direct consequence of the low aspect ratio $A = 2.5$ and the strong elongation $\kappa = 2.0$ — and they exceed the naive circular-cross-section estimate at the same r/a. A large trapped fraction is what makes the bootstrap current substantial in an ST, and it is also what makes the accurate treatment of the trapped-passing boundary (where NEO and the analytic fits part company) worth the kinetic solve.

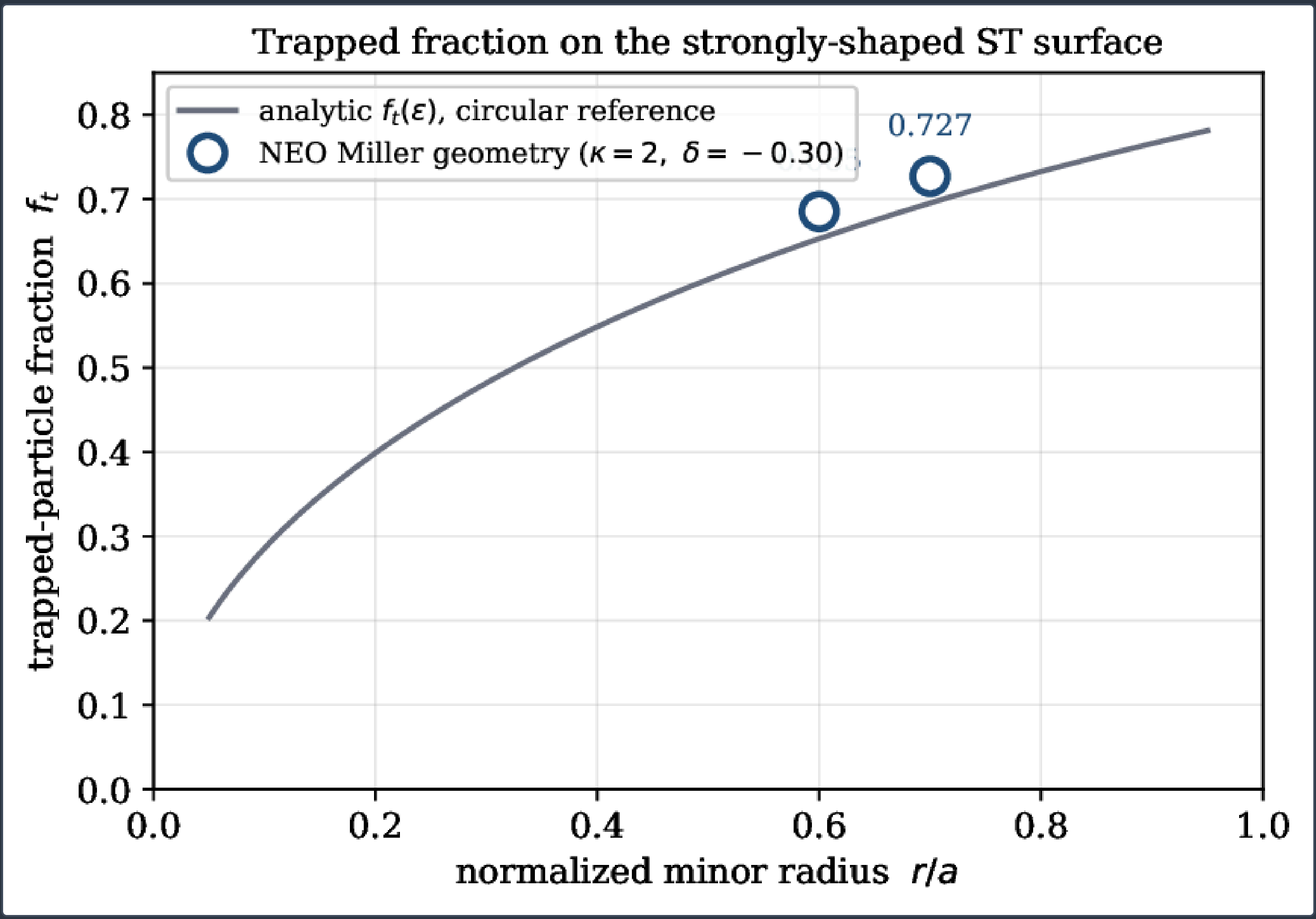

Trapped-particle fraction. The NEO-computed values on the shaped Miller surface ($\kappa = 2.0$, $\delta = -0.30$; blue markers) lie above the circular-cross-section analytic reference (grey), reflecting the large trapped population of the compact, strongly-shaped ST.

§ 5

Poloidal flows and impurity screening

NEOCLASSICAL POLOIDAL FLOW

The same drift-kinetic solve that returns the bootstrap current returns the neoclassical parallel and poloidal flows self-consistently, as the appropriate velocity moments of the solved g_a. In the banana-regime core the main-ion poloidal flow follows equation (9) with the classical coefficient $k_i \simeq 1.17$: the flow is proportional to, and directed by, the ion temperature gradient. This neoclassical flow is the collisional baseline on top of which the turbulence-driven and externally-driven rotation of the companion rotation study [29] sits, and it is the flow that enters the impurity balance below. Because the density is flat at the frozen operating point ($\partial \ln n/\partial r = 0$), the poloidal flow at these surfaces is set essentially by the temperature gradient alone, which cleanly isolates the screening term.

TEMPERATURE SCREENING AND THE COLLISIONALITY REGIME

The impurity flux of equation (10) contains the competition between the density-gradient pinch and the temperature-screening flux, sketched in figure 7. The sign of the screening coefficient $H(\nu_*)$ is regime-dependent: in the banana regime $H > 0$ and the ion temperature gradient drives impurities *outward*, opposing accumulation. The breeder core collisionality $\nu_*^e \approx 0.012$ places it firmly in that screening-favorable regime. Physically, the compact, high-temperature, low-collisionality core of the Kronos breeder is the regime in which temperature screening is strongest, which is a favorable — not adversarial — setting for high-Z impurity control, provided the ion temperature stays peaked relative to the density. The drift-kinetic framework used here is the one that quantifies $H(\nu_*)$ and D_z directly on a full multi-species profile [10,11]; the present local solve establishes the regime and the sign, and the full-profile multi-species run is the confirming calculation.

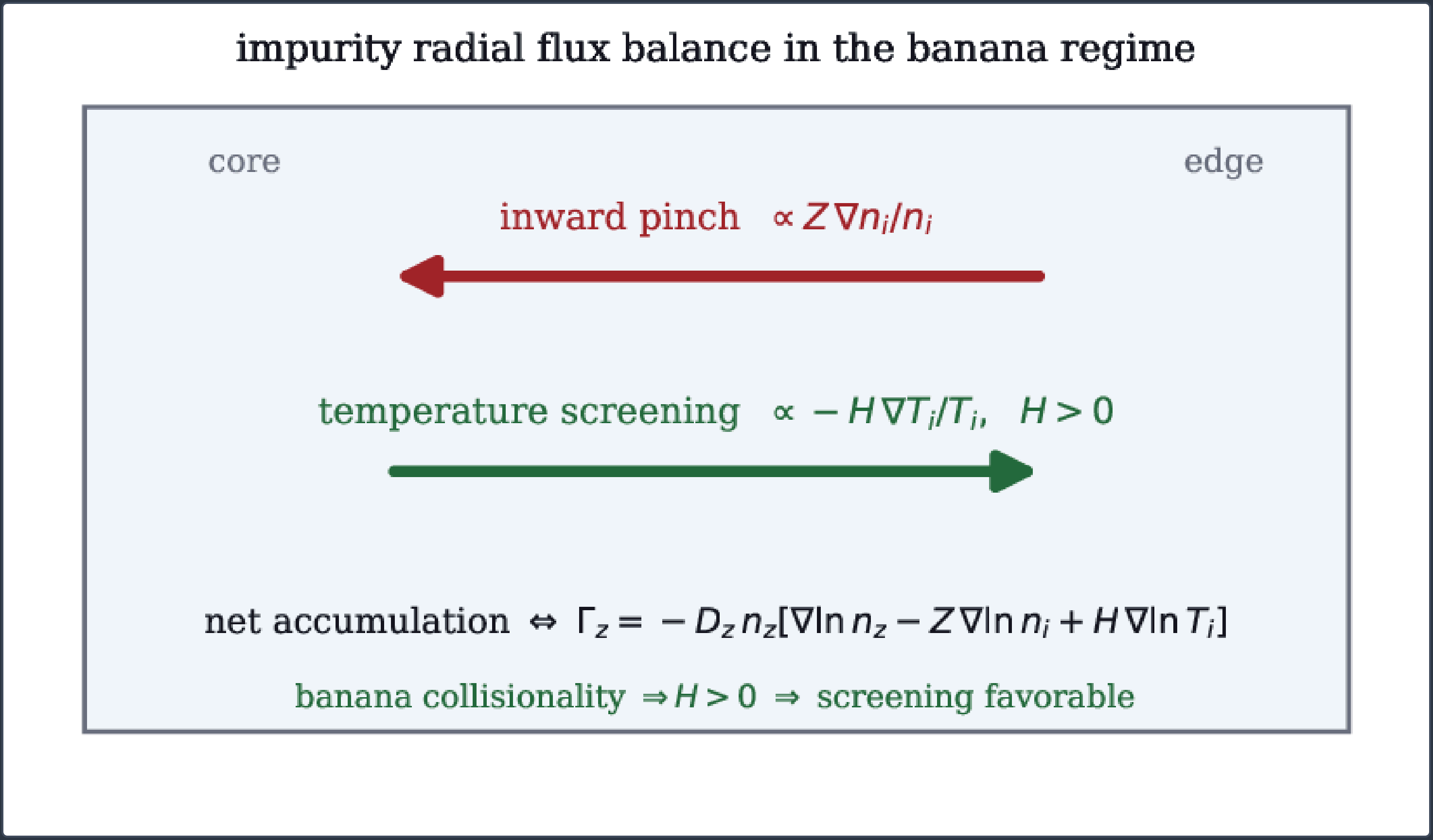

(Schematic.) Neoclassical impurity radial-flux balance in the banana regime: the inward pinch driven by the main-ion density gradient (red) competes against the outward temperature-screening flux (green). At the breeder core collisionality the screening coefficient $H > 0$, so a peaked ion-temperature profile opposes high-Z accumulation.

COUPLING TO THE RADIATED-POWER BUDGET

Temperature screening keeps impurities out; the collisional–radiative cooling curves say how much a given residual concentration would cost in radiated power. Independent ADAS collisional–radiative calculations (radas; serial BR-L2-A29 [13]) give the impurity cooling functions at the 15 keV core: $L_z^W = 5.7 \times 10^{-32}$ W m^3 for tungsten (mean charge $\langle Z \rangle = 61.9$) and $L_z^{\rm Ar} = 1.45 \times 10^{-33}$ W m^3 for argon — tungsten radiating roughly forty times harder per ion in the core. Folding these against the frozen profiles bounds the tolerable concentration (figure 8): the tungsten sensitivity is ≈ 0.19 MW per ppm, so holding the core tungsten concentration to $c_W \lesssim 3$ ppm keeps the impurity radiated-power add-on below ~ 0.6 MW (a small fraction of the core radiated power), while argon — a far softer core radiator — is tolerable at the several-hundred-ppm level. The neoclassical screening regime and the radiative tolerance therefore tell a consistent story: the core physics favors impurity exclusion, and the radiative budget sets a few-ppm ceiling on the high-Z residue the screening must hold. The core and edge radiated-power budget is closed in the companion collisional–radiative study [30].

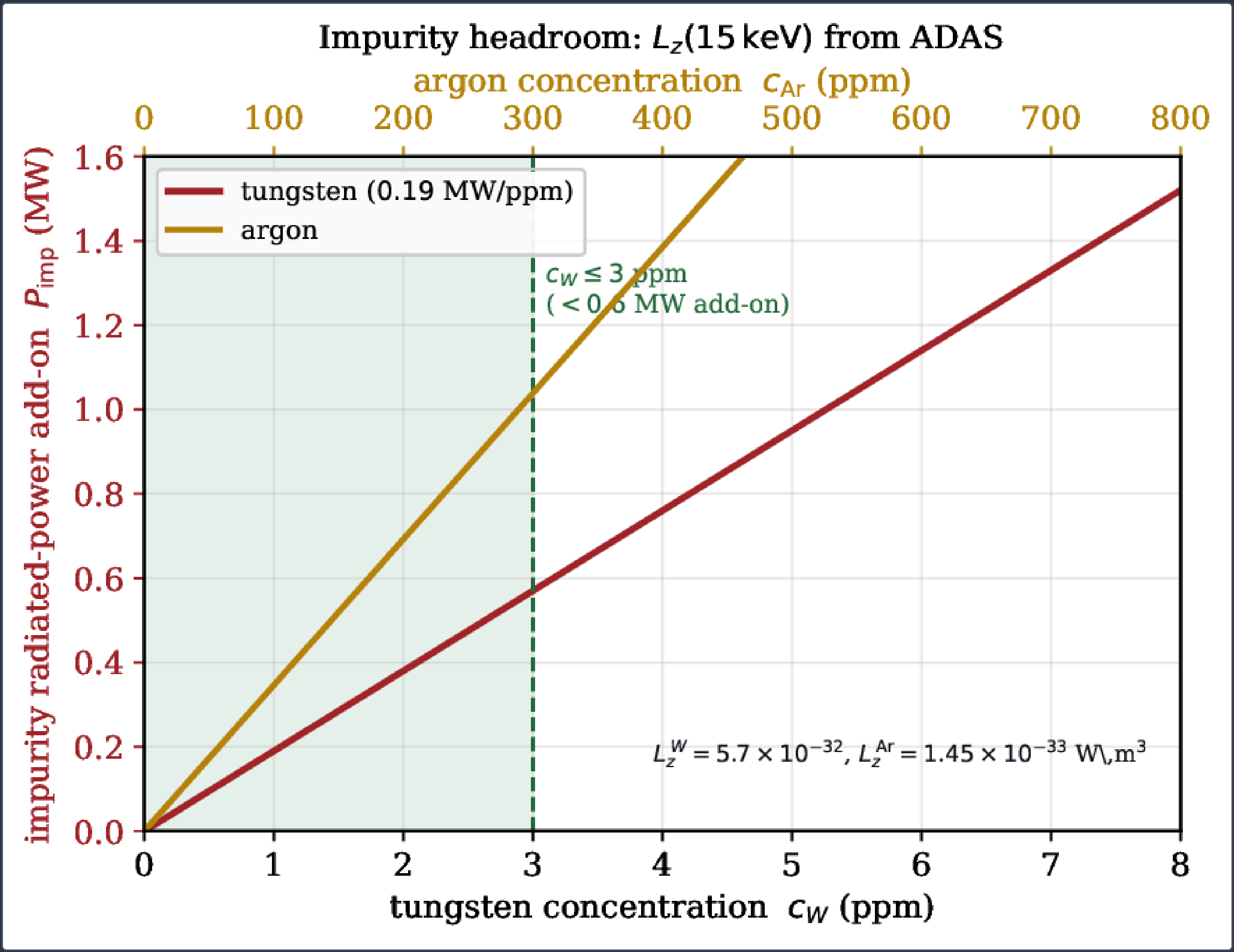

Impurity radiated-power headroom from ADAS collisional–radiative cooling curves (serial BR-L2-A29). Tungsten (red, lower axis) adds ≈ 0.19 MW ppm^{-1}; holding $c_W \lesssim 3$ ppm keeps the add-on below ~ 0.6 MW. Argon (gold, upper axis) is a far softer core radiator and tolerable at hundreds of ppm.

§ 6

GPU-accelerated HPC methodology

CODES RUN FOR THIS STUDY

The neoclassical results were produced on the Kronos NVIDIA GPU HPC campaign, the same verification-grade computing programme that carries the breeder physics de-risking set. For *this* paper the primary solver is NEO (GACODE) [6,7], run as a drift-kinetic local solve at three flux surfaces with the full linearized Fokker–Planck collision operator and kinetic electrons. The analytic-model comparison (Sauter [3], Koh [8], modified-Sauter and the Hirshman–Hinton banana limit [1]) is evaluated in the same GACODE theory module so that the drift-kinetic and analytic bootstrap currents share an identical geometry and normalization, and the impurity cooling functions are computed with radas over the ADAS ADF11 collisional–radiative data [13]. The turbulent transport this collisional baseline underlies was computed with the nonlinear gyrokinetic code CGYRO [16,17] on the same campaign and is reported in the companion negative- triangularity study [25]; the neoclassical baseline and the turbulent transport are the two halves of the same confinement picture.

GPU ACCELERATION, PROBLEM SCALE AND VERIFICATION

The neoclassical drift-kinetic solve assembles the block-sparse operator of equation (11) — with the velocity-space resolution $N_\varepsilon \times N_\xi \times N_\theta = 8 \times 17 \times 25$ per surface for a two-species (kinetic-electron, DT-ion) system — and factors it once with a sparse direct LU solver per surface; the neoclassical problem is modest in scale and memory-bound rather than throughput-bound, and it is the surrounding nonlinear-gyrokinetic and neutronics campaigns that consume the bulk of the GPU fleet's throughput. The GACODE suite is GPU-accelerated across the campaign's NVIDIA A100/H100/A10 nodes, and the neoclassical solves were carried within that environment so that the analytic-model comparison, the CGYRO turbulence runs and the neoclassical baseline all share a single, version-pinned toolchain. Reproducibility is enforced at the register level: the config-22021 anchor, the NEO input decks, and the driver that generates the three-surface sweep are archived with the deposit, the run is stamped with the exact GACODE build, and an independent re-run reproduces the NEO-to-Sauter ratio (register verdict: reproduced). The verification-first methodology — frozen anchors, independent-library gate reproduction, and a byte-for-byte provenance catalog — is described in the companion verification study [31]. No compute-cost information is reported; the campaign is referred to only by the codes it ran and the scale of the problems it solved.

§ 7

Discussion

THE RESULT AGAINST THE NEOCLASSICAL LITERATURE

The central quantitative finding — a drift-kinetic bootstrap current $0.81\text{–}0.87\times$ the Sauter analytic value in a deep-banana core — is exactly the direction and magnitude the neoclassical literature predicts. Comparisons of the Sauter formulas against dedicated numerical solvers have repeatedly shown the analytic fit to over-predict the bootstrap current at low collisionality and in strongly-shaped or steep-gradient regions, motivating the Redl *et al.* recalibration [5] and the Koh edge-pedestal treatment [8]. Our result reproduces that picture from first principles on a compact-ST operating point that the original Sauter database did not cover, and it quantifies the correction (a $\sim 17\%$ reduction at mid-radius) rather than merely flagging it. The trapped fractions $f_t = 0.685\text{–}0.727$ we compute are consistent with the large trapped populations expected at $A = 2.5$ and $\kappa = 2.0$, and they are what make the bootstrap current both large and sensitive to the trapped-passing physics that distinguishes NEO from the fits.

IMPURITY SCREENING IN CONTEXT

The impurity picture is likewise consistent with the modern understanding of neoclassical impurity transport. The banana-regime temperature-screening mechanism [2,10] predicts that a low-collisionality, temperature-peaked core opposes high-Z accumulation, and recent negative-triangularity experiments on DIII-D report flat or hollow core impurity profiles and impurity confinement times shorter than the energy confinement time [12] — i.e. favorable core impurity behavior in the same shape class as the Kronos point. Our computed core collisionality places the breeder in that screening-favorable regime, and the ADAS cooling-curve coupling turns the qualitative regime statement into a quantitative few-ppm tungsten ceiling. The consistency of the two independent lines — the drift-kinetic screening regime and the collisional–radiative radiated-power budget — is the point: they agree that the compact breeder core is a favorable, not adversarial, setting for high-Z control, with a well-defined tolerance.

CONSEQUENCES FOR THE DESIGN POINT

Grounding the bootstrap current in kinetic theory changes it from an assumption into a measured quantity with a stated uncertainty. The current-drive burden implied by $f_{\text{bs}} = 0.155$ — an external-drive requirement of $\simeq 8.2$ MA — now rests on a calculation whose model uncertainty is bounded by the solve rather than by the factor-of-two spread across analytic fits, and the companion current-drive and solenoid-free-startup studies [27,28] inherit that bounded baseline. The same framework carries the poloidal flows and the temperature-screening mechanism, so the impurity-transport question sits on the same first-principles footing. The collisional baseline is now in place beneath the turbulent transport that sets the confinement.

§ 8

Limitations

One honest gate bounds the claims. The bootstrap *ratio* to Sauter is a clean first-principles result: it is a local, geometry-consistent comparison at each surface, insensitive to the profile-integration and normalization approximations. The integrated *magnitude* $f_{\rm bs} = 0.155$ is a different object. A crude three-surface profile integral of the local NEO current, with the flat density that suppresses the ∇n drive and an approximate field normalization, returns $f_{\rm bs} \sim 0.075$–0.087 — roughly a factor of two below the toolkit anchor. This is not a refutation of 0.155: the discrepancy is within what the flat-density profile ($\partial \ln n / \partial r = 0$ kills a real gradient drive), the three-point integration, the $\langle j_\parallel B \rangle / B_{\rm unit}$-as-$j_\parallel$ approximation, and the approximate $B_{\rm unit}$ can explain, and the integrated toolkit value carries the geometry the local mapping drops. The confirming calculation for the absolute fraction — and for the quantitative impurity flux Γ_z — is a full-profile, multi-species NEO run from a converged free-boundary equilibrium (an `input.gacode` built from the FreeGS/CHEASE geometry for $\delta = -0.30$ [19,18], with proper flux-surface integration of the toroidal current). That run is the natural follow-on; the present study fixes the ratio, the regime, and the sign of the screening, which are the load-bearing conclusions.

§ 9

Conclusion

A drift-kinetic NEO solve on the negative-triangularity Kronos breeder point returns a parallel bootstrap current 0.81–$0.87\times$ the Sauter analytic value across the mid-radius (0.843 at $r/a = 0.6$), reproducing the de-risking register's $\sim 83\%$-of-Sauter anchor from first principles and explaining the offset as the expected banana-regime correction at $\nu_*^e \approx 0.012$ — a correction that shrinks monotonically toward unity as collisionality rises outward, the signature of real low-collisionality physics rather than a numerical artifact. The same solve delivers the large trapped fractions of the compact, strongly-shaped ST ($f_t = 0.685$–0.727), the neoclassical poloidal flows, and the temperature-screening mechanism, and it places the breeder core in the screening-favorable banana regime; coupling that regime to independent ADAS collisional–radiative cooling curves bounds the tolerable tungsten concentration at a few ppm. With the bootstrap ratio anchored in kinetic theory, the integrated fraction pinned at $f_{\mathrm{bs}} = 0.155$ pending a full-profile confirmation, and the impurity screening quantified, the neoclassical transport of the compact breeder is now a grounded collisional baseline — with a stated model uncertainty — beneath the turbulent transport that sets the confinement.

Acknowledgments tocsectionAcknowledgments Part of the Kronos Fusion Energy 2026 design series. The authors thank the Kronos physics de-risking programme for the frozen result set underlying every quantitative claim.

Reproducibility. The neoclassical results are frozen anchors in the Kronos Physics De-Risking Register [24] (doi:10.5281/zenodo.22133057): the first-principles NEO drift-kinetic solve (BR-L2-A16), the integrated bootstrap fraction (BR-L2-A6), and the ADAS impurity cooling curves (BR-L2-A29). They were computed with NEO (GACODE) and radas on the config-22021 anchor and are regenerable from the archived driver, NEO input decks and version stamp deposited with this paper; this paper is archived at doi:10.5281/zenodo.22645832; official version: https://www.kronosfusionenergy.com/publications/neoclassical-transport-poloidal-flows-and-impurity-scre.html.

Data availability tocsectionData availability The NEO inputs and outputs, the analytic-model comparison, and the ADAS cooling-curve data used for the figures are archived with the deposit at doi:10.5281/zenodo.22645832, which references the Kronos 2026 series. All quantitative values trace to the register [24] by the serial identifiers cited inline. Any economic analysis is reported separately and is not part of the public deposit.

Competing interests tocsectionCompeting interests Provisional patent applications relating to aspects of this work have been filed.

tocsectionReferences

APPARATUS

Portfolio, People & Record

The intellectual-property estate, the people who built it, the limitations that gate it, and the sources it rests on.

1	4	40	27
GRANTED PATENT	2026 PROVISIONALS	TEAM MEMBERS	2022 PROVISIONALS

INTELLECTUAL PROPERTY

The patent portfolio

The estate spans a granted high-field magnet patent, pending utility and 2026 provisional filings that map to the two products, a digital-twin control provisional, a registered trademark application, and the original 2022 provisional family. Every patentable disclosure in the five-paper arXiv drop was protected **before** publication: the breeder and burner provisionals were filed 1–2 August, and a publication-gap omnibus filing the evening before the drop swept up the DEC, plasma-control, and REBCO-winding matter of the three otherwise-unprotected papers. Patent numbers and application serials are matters of public record; claim scope is summarised, not reproduced.

GRANTED & PENDING UTILITY

US 12,009,112	High-field tilted graded-REBCO magnet architecture (KRONO-002A) *· app. 17/878,550*	GRANTED
US 17/878,507	Core device / method (KRONO-001A) *· utility*	PENDING

2026 PROVISIONAL FILINGS — MAPPED TO THE PRODUCTS

64/124,209	Hyperion — spherical-tokamak tritium / helium-3 foundry *· breeder · filed Aug 2026*	FILED
64/124,220	Aegis / MetroVolt — synchrotron-cutoff, fuel-selection & plug-winding *· generator · filed Aug 2026*	FILED
64/115,167	KRONOS-CTRL digital-twin plant control *· provisional · filed Jul 2026*	FILED
64/005,440	Integrated spherical-tokamak fusion architecture *· early integrated-architecture filing · filed Mar 2026*	FILED
64/105,530	Negative-triangularity spherical-tokamak architecture *· foundational ST filing · filed Jul 2026*	FILED
64/128,097	Publication-gap omnibus — quasineutral two-species expander DEC · provenance-gated / latency-split plasma control · as-built high-field winding & conductor architecture *· filed 7 Aug 2026, the evening before the arXiv drop*	FILED

TRADEMARK & ORIGIN

FTK-98801894	Kronos Fusion Energy — trademark application	FILED
KR-2022-*	Original provisional family (KR-2022-00001 … 00027) *· 27 filings, 2022*	PRIORITY

The narrow, defensible magnet novelty — the specific conductor and the digital-twin winding optimisation, not high-field REBCO as a category — is the commercial core that can earn ahead of any Q > 1 milestone, with markets in fusion magnet supply, MRI/NMR, accelerators, and proton therapy. The claim is scoped honestly: the high field is a *system field* result, not a stand-alone-coil record; the small-bore plug coil is structurally infeasible as a bare winding but resolved by a stress-managed structural shield (feasible-pending-FEA); and the winding-tape experiment returned a *null result*. The value is the method, not a field record.

THE TEAM

Founding partners, board, advisors & auditors

Kronos is built by a bench of advanced-fuel-fusion, high-field-magnet, direct-conversion, and materials specialists, with a board and operations team drawn from defense, national laboratories, and industry. Dates are shown as ranges; where a tenure has ended or is term-ending, the range says so.

FOUNDING PARTNERS — SCIENCE

Dr. Gerald Kulcinski
Co-Founder · Helium-3 & Advanced-Fuel Fusion
UW–Madison · 2023–Present

Dr. Carl Weggel
Chief Scientist / S.M.A.R.T. Design
MIT Alcator Program · 2022–Present

Dr. Robert J. Weggel
Magnetic Field Design
MIT Magnet Lab · 2022–Present

BOARD

Priyanca Ford
Founder & CEO · Executive Board
2022–Present

Bandel Carano
Finance / Strategy
Oak Investment Partners / Stanford · 2025–2026

Patrick Schweiger
Fusion Device Engineering
Oklo / CFS / TerraPower · 2025–Present

SCIENTIFIC ADVISORS

Dr. Steven O. Dean
Fusion Policy & History
DOE / Fusion Power Associates · 2025–Present

Dr. Patrick H. Diamond
Plasma Turbulence & Transport
UC San Diego · 2025–Present

Dr. Jack J. Dongarra
HPC & Numerical Algorithms
Turing Award · 2025–Present

Dr. Nasr M. Ghoniem
Chief Material Scientist
UCLA · 2025–Present

Dr. Siegfried Glenzer
Plasma Physics & Laser Fusion
Stanford / SLAC · 2022–Present

Dr. David A. Hammer
Pulsed-Power Fusion
Cornell · 2025–Present

Dr. Donald A. Spong
Plasma Theory & Confinement
ORNL · 2025–Present

Dr. Curtis Smith
Risk Assessment & Nuclear PRA
MIT / Idaho National Lab · 2025–Present

RADM (Ret.) David Goggins
Naval Engineering & Power-Plant Design
U.S. Navy · 2023–2026

Dr. Konstantin Batygin
Mathematician
Caltech · 2022–2025

Dr. Ruben Fair
Magnet Design / ITER Liaison
PPPL / Jefferson Lab · 2022–2025

Dr. Paul S. Weiss
Materials & Nanotechnology
UCLA · 2022–2025

SCIENTIFIC AUDITORS

Dr. Wilfred A. Cooper
Plasma Equilibrium Theory
EPFL / Swiss Plasma Center · 2025–Present

Dr. Ahmed Hassanein
Plasma–Material Interactions
Purdue / Argonne · 2025–Present

Dr. Patrick E. Hopkins
Extreme Thermal Materials
U. of Virginia · 2025–Present

Dr. Peter Hosemann
Materials Joining & Structural Integrity
UC Berkeley · 2025–Present

Dr. Travis W. Knight
Advanced Nuclear Fuels & Systems
U. of South Carolina · 2025–Present

Dr. Philippe Lebrun
Cryogenics & Magnet Cooling
CERN · 2025–Present

Dr. Nitendra Singh
Nuclear Safety & Fuel Cycle
ITER · 2025–Present

Dr. Guido Van Oost
Magnetic Confinement & Fusion Systems
Ghent University · 2025–Present

Dr. Gary S. Was
Radiation Materials & Structural Integrity
U. of Michigan · 2025–Present

Dr. Ray Sedwick
Direct Energy Conversion
U. of Maryland · 2025

OPERATIONS

Michael Laughlin
Chief Operating Officer
2022–Present

Martin Owens
Chief Strategy Officer
LANL / GE Hitachi · 2022–Present

MG (Ret.) Paul Pardew
Chief Contracting Officer
Army Contracting Command · 2022–Present

David Beck
Fusion Commercialization
U.S. Space Force · 2024–Present

Sushma Bhatia
Environmental & Legislative
Google · 2022–Present

Michael De Frenza
Technology Licensing
2023–Present

MG (Ret.) Robin L. Fontes
Cybersecurity & Defense
Army Cyber Command · 2022–Present

Vijay Gehani
Supply Chain & Components
INOX India · 2024–Present

Jon Michel Greenwood
IT & AI Infrastructure
Live Nation · 2023–Present

Brian C. O'Neill
National Security
CIA / ODNI · 2022–Present

Gen. (Ret.) Gustave F. Perna
DoD Liaison
Operation Warp Speed · 2022–2023

Andrea Romero
Marketing Lead
2022–Present

Legal counsel is retained; those roles are held on the internal roster and are not listed here.

SOURCES

References

1 F L Hinton and R D Hazeltine, Theory of plasma transport in toroidal confinement systems, *Rev. Mod. Phys.* **48** 239 (1976). doi:10.1103/RevModPhys.48.239

2 S P Hirshman and D J Sigmar, Neoclassical transport of impurities in tokamak plasmas, *Nucl. Fusion* **21** 1079 (1981). doi:10.1088/0029-5515/21/9/003

3 O Sauter, C Angioni and Y R Lin-Liu, Neoclassical conductivity and bootstrap current formulas for general axisymmetric equilibria and arbitrary collisionality regime, *Phys. Plasmas* **6** 2834 (1999). doi:10.1063/1.873240

4 O Sauter, C Angioni and Y R Lin-Liu, Erratum: Neoclassical conductivity and bootstrap current formulas for general axisymmetric equilibria and arbitrary collisionality regime, *Phys. Plasmas* **9** 5140 (2002). doi:10.1063/1.1517052

5 A Redl, C Angioni, E Belli, O Sauter (ASDEX Upgrade Team and EUROfusion MST1 Team), A new set of analytical formulae for the computation of the bootstrap current and the neoclassical conductivity in tokamaks, *Phys. Plasmas* **28** 022502 (2021). doi:10.1063/5.0012664

6 E A Belli and J Candy, Kinetic calculation of neoclassical transport including self-consistent electron and impurity dynamics, *Plasma Phys. Control. Fusion* **50** 095010 (2008). doi:10.1088/0741-3335/50/9/095010

7 E A Belli and J Candy, Full linearized Fokker–Planck collisions in neoclassical transport simulations, *Plasma Phys. Control. Fusion* **54** 015015 (2012). doi:10.1088/0741-3335/54/1/015015

8 S Koh, C S Chang, S Ku, J E Menard, H Weitzner and W Choe, Bootstrap current for the edge pedestal plasma in a diverted tokamak geometry, *Phys. Plasmas* **19** 072505 (2012). doi:10.1063/1.4736953

9 A G Peeters, The bootstrap current and its consequences, *Plasma Phys. Control. Fusion* **42** B231 (2000). doi:10.1088/0741-3335/42/12B/318

10 C Angioni, Impurity transport in tokamak plasmas, theory, modelling and comparison with experiments, *Plasma Phys. Control. Fusion* **63** 073001 (2021). doi:10.1088/1361-6587/abfc9a

11 F J Casson, C Angioni, E A Belli, R Bilato *et al*, Theoretical description of heavy impurity transport and its application to the modelling of tungsten in JET and ASDEX Upgrade, *Plasma Phys. Control. Fusion* **57** 014031 (2015). doi:10.1088/0741-3335/57/1/014031

12 F Sciortino, N T Howard, T Odstrcil *et al*, Investigation of core impurity transport in DIII-D diverted negative triangularity plasmas, *Plasma Phys. Control. Fusion* **64** 124002 (2022). doi:10.1088/1361-6587/ac94f6

13 H P Summers, W J Dickson, M G O'Mullane *et al*, Ionization state, excited populations and emission of impurities in dynamic finite density plasmas: I. The generalized collisional–radiative model for light elements, *Plasma Phys. Control. Fusion* **48** 263 (2006). doi:10.1088/0741-3335/48/2/007

14 R L Miller, M S Chu, J M Greene, Y R Lin-Liu and R E Waltz, Noncircular, finite aspect ratio, local equilibrium model, *Phys. Plasmas* **5** 973 (1998). doi:10.1063/1.872666

15 Y B Kim, P H Diamond and R J Groebner, Neoclassical poloidal and toroidal rotation in tokamaks, *Phys. Fluids B* **3** 2050 (1991).

16 J Candy and R E Waltz, An Eulerian gyrokinetic-Maxwell solver, *J. Comput. Phys.* **186** 545 (2003). doi:10.1016/S0021-9991(03)00079-2

17 J Candy, E A Belli and R V Bravenec, A high-accuracy Eulerian gyrokinetic solver for collisional plasmas, *J. Comput. Phys.* **324** 73 (2016). doi:10.1016/j.jcp.2016.07.039

18 F Felici *et al*, Real-time physics-model-based simulation of the current density profile in tokamak plasmas, *Nucl. Fusion* **51** 083052 (2011). doi:10.1088/0029-5515/51/8/083052

19 N C Amorisco *et al*, FreeGSNKE: a Python-based dynamic free-boundary toroidal plasma equilibrium solver, *Phys. Plasmas* **31** 042517 (2024). doi:10.1063/5.0188467

20 J E Menard *et al*, Fusion nuclear science facilities and pilot plants based on the spherical tokamak, *Nucl. Fusion* **56** 106023 (2016). doi:10.1088/0029-5515/56/10/106023

21 B N Sorbom *et al*, ARC: a compact, high-field, fusion nuclear science facility and demonstration power plant with demountable magnets, *Fusion Eng. Des.* **100** 378 (2015). doi:10.1016/j.fusengdes.2015.07.008

22 M E Austin *et al*, Achievement of reactor-relevant performance in negative triangularity shape in the DIII-D tokamak, *Phys. Rev. Lett.* **122** 115001 (2019). doi:10.1103/PhysRevLett.122.115001

23 A Marinoni, O Sauter and S Coda, A brief history of negative triangularity tokamak plasmas, *Rev. Mod. Plasma Phys.* **5** 6 (2021). doi:10.1007/s41614-021-00054-0

24 P I Ford, *The Physics De-Risking Register: Gate-by-Gate Evidence, Independently Re-Run and Stamped*, Kronos Fusion Energy 2026 series. doi:10.5281/zenodo.22133057

25 P I Ford and G L Kulcinski, *Negative-Triangularity Turbulence Suppression in a Compact Spherical-Tokamak Breeder: Nonlinear Gyrokinetics of Ion- and Electron-Scale Quiescence at the Operating Point*, Kronos Fusion Energy 2026 series. doi:10.5281/zenodo.22645722

26 P I Ford, *Two-Code Cross-Validation of Negative-Triangularity Turbulence Suppression: Quasilinear TGLF Confirms Nonlinear CGYRO*, Kronos Fusion Energy 2026 series. doi:10.5281/zenodo.22645864

27 P I Ford and G L Kulcinski, *Bootstrap-Aligned Steady-State Current Sustainment Without a Central Solenoid: NBCD, ECCD and LHCD for a Compact Spherical-Tokamak Breeder*, Kronos Fusion Energy 2026 series. doi:10.5281/zenodo.22645758

28 P I Ford and G L Kulcinski, *From Breakdown to Flat-Top: Solenoid-Free Startup and Disruption-Free Ramp Access for a Negative-Triangularity Spherical-Tokamak Breeder*, Kronos Fusion Energy 2026 series. doi:10.5281/zenodo.22645760

29 P I Ford and G L Kulcinski, *Toroidal Rotation, Flow-Shear Stabilization and Error-Field Correction in a Compact Spherical-Tokamak Breeder: Residual Transport and Locked-Mode Avoidance*, Kronos Fusion Energy 2026 series. doi:10.5281/zenodo.22645907

30 P I Ford and G L Kulcinski, *Collisional-Radiative Impurity-Radiation Modeling for a Compact Spherical-Tokamak Breeder: Closing the Core and Edge Radiated-Power Budget*, Kronos Fusion Energy 2026 series. doi:10.5281/zenodo.22645883

31 P I Ford, *Verification-First Fusion Modeling: Frozen Anchors, Independent-Library Gate Reproduction, and a Byte-for-Byte Computational-Provenance Catalog*, Kronos Fusion Energy 2026 series. doi:10.5281/zenodo.22645710

COLOPHON

How this document was made

The Kronos Fleet — Combined Editorial, 2026 is set in **Fraunces** (display), **Gelasio** (text), and **IBM Plex Mono** (data & equations), carried forward from the Kronos editorial design system.

The figures are rendered at 300 dpi from the deposited generator scripts; the document is composed as a single self-contained file with embedded fonts and imagery, paginated to US Letter, and rendered to PDF through a headless Chromium engine in matched light and dark editions.

Every headline quantity carries an evidence class; withdrawn and restated values are marked as such. Nothing herein is frozen beyond the founder-approved Tier-A set.

Explore it live — turn the interactive 3-D model, run the deposited solvers in the physics validator, and watch the companion film series.

LEGAL NOTICE

Notice, status, and distribution

Conceptual design & simulation study. This document reports a conceptual design and simulation study. It is not a construction commitment, a safety-analysis report, a regulatory filing, or an offer of securities. Forward-looking statements — schedules, costs, market sizes, and performance — are estimates subject to the limitations set out in the Simulations part and may change.

Numbers and their classes. Quantities are reported with evidence classes and case labels; modelled, assumed, and requirement-class values are identified as such and are not to be quoted without their labels.

Public edition. This edition carries the physics and design only; all financial, funding, and defense-commercial content has been removed for public distribution. The scientific text corresponds to the arXiv and journal submissions.

THE 2026 KRONOS SERIES

One programme, many papers

This editorial is one paper in the Kronos 2026 series — a real fusion company's complete, reproducible physics record for a spherical-tokamak breeder and its low-neutron D–^{3}He tandem-mirror burners. Every headline number is a frozen anchor in the Physics De-Risking Register.

Explore the whole programme: the De-Risking Register, the interactive 3-D model, and the physics validator.

KRONOS FUSION ENERGY

Neoclassical Transport, Poloidal Flows, and Impurity Screening in a Compact Spherical-Tokamak Breeder: The Collisional Baseline Beneath Turbulent Transport

A real fusion company building real machines. Explore the science, live.

Zenodo · doi:10.5281/zenodo.22645832

Read on kronosfusionenergy.com

The Physics De-Risking Register